

Anion intercalation enables efficient and stable carboxylate upgrading via aqueous non-Kolbe electrolysis

Received: 25 September 2024

Accepted: 2 April 2025

Published online: 19 April 2025



Xinyan Zhang^{1,2,4}, Laihao Luo^{1,2,4}, Chunxiao Liu^{1,2,4}, Weiqing Xue^{1,2}, Yuan Ji², Donghao Zhao¹, Pengbo Liu¹, Xinran Feng², Jun Luo¹, Qiu Jiang^{1,2}, Tingting Zheng^{1,2}, Xu Li^{1,2}, Chuan Xia^{1,2}✉ & Jie Zeng^{1,3}✉

Next-generation techniques for sustainable carboxylate production generate carboxylate salts as the primary outcome. To circumvent the costly conversion of carboxylate salts to acids, we demonstrate the aqueous (non-)Kolbe electrolysis process as an alternative strategy to generate downstream value-added chemicals. Upon revealing the irreversible oxidation-induced charge transfer inhibition on the graphite anode, we propose an anion intercalation strategy to mitigate the stability problem induced by the ever-increasing overpotential. In acetate decarboxylation, we observe a high Faradaic efficiency of ~95% for non-Kolbe products (methanol and methyl acetate) at wide current densities ranging from 0.05 to 1 A cm⁻² and long-term stability at current densities of 0.15 and 0.6 A cm⁻² for 130 and 35 h, respectively. We also extended this strategy for the upgrading of long-chain carboxylates such as propionate, butyrate, and succinate. Our work provides valuable guidance for carboxylate upgrading and extendable strategy for overcoming passivation challenges in catalysis.

In recent years, there has been significant progress in the production of carboxylate salts, which are generated primarily through sustainable processes such as carbon dioxide and carbon monoxide (CO_x) electroreduction^{1,2}, waste plastic degradation^{3,4}, and biomass conversion⁵. Although there have been notable advancements in the production of carboxylates, the transformation from salt to acid remains an energy-intensive process, which could undermine the goal of achieving a carbon-neutral cycle⁶. Concurrently, various thermal^{7,8}, electrochemical^{9,10}, and photochemical^{11,12} methods for the catalytic upgrading of carboxylate salts or carboxylic acids have undergone rapid development. Among these, electrochemical methods are particularly noteworthy due to their mild operation conditions, high efficiency, and integration with renewable energy sources^{13,14}. The electrochemical transformation of carboxylic acids, widely recognized

as Kolbe electrolysis, can be traced back to the 19th century^{15,16}. In this process, the carboxylates lose electrons at the anode, forming alkyl radicals. These active radicals either dimerize to Kolbe products (paraffin) or undergo further oxidation to carbocations, leading to the production of valuable non-Kolbe products such as olefins, alcohols, and esters^{17–19}. Despite extensive research spending over a century, the applications of this reaction remain limited due to its strictly restricted solvation conditions and inevitable stability challenges^{20–22}.

For a sustainable future, developing an efficient strategy to direct non-Kolbe electrolysis in aqueous electrolytes to upgrade the carboxylates produced via green chemistry routes is attractive. Although several studies have investigated aqueous phase non-Kolbe electrolysis using carboxylate salts as reactants, they have encountered challenges such as low Faradaic efficiency and diminished reactivity

¹Hefei National Research Center for Physical Sciences at the Microscale, University of Science and Technology of China, Hefei, Anhui, China. ²School of Materials and Energy, University of Electronic Science and Technology of China, Chengdu, China. ³School of Chemistry & Chemical Engineering, Anhui University of Technology, Ma'anshan, Anhui, China. ⁴These authors contributed equally: Xinyan Zhang, Laihao Luo, Chunxiao Liu.

✉ e-mail: chuan.xia@ustc.edu.cn; zengji@ustc.edu.cn

toward the desired products, particularly when employing graphite anodes^{23–28}. It has also been reported that the involvement of anions could lead to a notable decrease in electrolysis efficiency²⁹. Another problem for the anode reaction lies in the stability of the catalyst materials. A high potential of more than 2 V *vs.* RHE is required for sufficient coverage of alkoxy or alkyl radicals to inhibit solvent oxidation³⁰. These substantial overpotentials can result in metal dissolution or passivation of the catalytically active surfaces^{31–34}. Promising erosion-resistant carbon-based catalysts such as boron-doped diamond (BDD) also suffer boron leaching and the graphitization of carbon at the grain boundaries during the decarboxylation process, especially at high operation current densities³⁵. Crucially, there is a lack of effective solutions to these stability issues, and the underlying mechanisms have not yet been fully elucidated. The regulation of electrolysis patterns, such as the adoption of square-wave polarization, offers another promising way to resolve activity or stability issues and has already been successfully demonstrated in various reactions^{34,36,37}. However, these strategies may lead to potential risks in the over-hydrogenation of the produced alkene products and energy loss during the charge-discharge cycles²⁶. The pursuit of understanding and overcoming these challenges is essential for advancing the field of carboxylate electrolysis.

Herein, we report an efficient anion intercalation strategy to increase the efficiency and stability of carboxylate upgrading via aqueous non-Kolbe electrolysis. Using acetate decarboxylation as a model system and employing graphite as the anode catalyst, we first conducted a thorough investigation of catalyst deactivation using spectroscopic techniques. Our findings indicated that irreversible oxidative damage to the graphite surface blocked the active sites and hindered electron transfer, thus inducing a significant increase in overpotential and a rapid decrease in both selectivity and activity. Then, we implemented an anion intercalation strategy, specifically by introducing perchlorate ions into the electrolyte. Remarkably, this intercalation method resulted in an extraordinarily high FE of ~95% for the generation of non-Kolbe products (methanol and methyl acetate) at wide current densities ranging from 0.05 to 1 A cm⁻². Furthermore, the intercalated graphite exhibited long-term stability at 0.15 and 0.6 A cm⁻² over 130 and 35 h, respectively. The intercalation of perchlorate ions preserved the electron transfer capabilities of graphite, leading to sustained and superior catalytic performance. In-situ spectroscopic studies revealed that perchlorate modulates both the adsorption and local concentration of acetate on the surface, thereby promoting alcohol production. Additionally, we observed long-term preservation of the initial catalytic activity across a variety of multiple carboxylates, including propionate, butyrate, succinate, and levulinate decarboxylation, upon the introduction of perchlorate ions. This confirms the broad potential and versatility of our intercalation strategy.

Results and discussion

Unraveling the deactivation mechanism of the anode catalyst

To determine the cause of deactivation during the aqueous non-Kolbe reaction, we employed acetate decarboxylation as a prototypical reaction and selected graphite as the anode catalyst due to its widespread use. The reaction parameters were carefully tuned, and a three-electrode flow cell was used as a reactor to avoid the influence of pH fluctuations and product accumulation (Supplementary Fig. S1, 2 and Supplementary Note 1). Initially, we evaluated the catalytic performance of graphite in a buffered solution containing 2 M acetate sodium (NaAc) and 2 M acetic acid (HAc) while maintaining a steady current density of 0.15 A cm⁻². As shown in Fig. 1a, graphite initially exhibited impressive performance (~100% non-Kolbe products), with a high Faradic efficiency (FE) for methanol and methyl acetate, as determined by ¹H nuclear magnetic resonance (NMR) (Supplementary Fig. 3). However, following approximately 2 h of electrolysis, the

potential rapidly increased from approximately 2.5 to 5 V *vs.* RHE, which was accompanied by a significant reduction in the catalytic selectivity from nearly 100% to approximately 45%.

We then compared the changes in the performance of graphite before and after deactivation over a wide range of current densities from 0.05 to 0.3 A cm⁻². Before deactivation, as shown in Fig. 1b, the graphite maintained a total FE of ~90% for methanol and methyl acetate at different current densities. In contrast, for graphite that had been deactivated at 0.3 A cm⁻², the FEs for all non-Kolbe products decreased to less than 50% under varying current densities (Fig. 1c). Additionally, we noted an apparent increase in the overpotentials triggered by deactivation across all tested current densities (Fig. 1d). Notably, trace gas products such as ethane (C₂H₆), carbon monoxide (CO), and oxygen (O₂) were detected by gas chromatography (GC) before deactivation, with FEs lower than 1% (Supplementary Figs. 4 and 5a). Post-deactivation, however, there was a considerable increase in C₂H₆ and CO, which accounted for ~5% of the FEs at elevated current densities. The augmented production of C₂H₆ can be ascribed to the accumulation of methyl radicals on the graphite surface at high potentials, whereas the generation of CO suggests the over-oxidation of non-Kolbe products. In-situ differential electrochemical mass spectrometry (DEMS) was implemented to track the variations in the gas products during the deactivation process. As illustrated in Supplementary Figs. 5b–d, subsequent to deactivation at 3000 s, there was a notable increase in C₂H₆ with increasing potential, which aligns with the online GC findings. The intensity of CO₂ initially escalated after deactivation, a trend that can be explained by the promotion of the one-electron process for C₂H₆ production, which generates more CO₂ molecules than the two-electron process does. In addition, we evaluated the performance of the deactivated graphite at a current density of 0.3 A cm⁻² under relatively high flow rates to exclude possible overoxidation of the products. The total FE of non-Kolbe products is maintained at ~40%, and there are limited variations in the potential. We, therefore conclude that the influence of the flow rate on the electrolytic performance is negligible (Supplementary Fig. 6).

Through comprehensive experimental analysis, we determined that the deactivation phenomena observed in graphite are physically irreversible, as evidenced by Supplementary Fig. 7. The degradation of the catalytic performance during electrolysis was likely due to the structural passivation of the active sites for decarboxylation. We employed X-ray diffraction (XRD) to elucidate the structural integrity of the deactivated graphite. The XRD patterns of pristine graphite displayed diffraction peaks at 26.4°, 44.6°, 54.7°, and 77.7°, which were identical to those of graphitic carbon. Post-deactivation analysis revealed negligible peak shifts, indicating the retention of the crystalline phase (Supplementary Fig. 8). Surface alterations were further investigated using Raman spectroscopy (Supplementary Fig. 9). Two peaks located at 1350 and 1580 cm⁻¹ were assigned to the D and G peaks of graphite, respectively³⁸, and exhibited an increase in the I_D/I_G ratio from 0.341 to 1.026 following deactivation, suggesting an increase in the number of defect sites. Scanning electron microscopy (SEM) imaging revealed a discernible loss of the layered structure of the graphite upon deactivation (Supplementary Fig. 10). To probe the surface oxidation states, X-ray photoelectron spectroscopy (XPS) was utilized (Fig. 1e). The C 1s spectra of pristine graphite exhibited three peaks at 284.8, 285.6, and 286.5 eV, corresponding to C=C, C-OH, and C-O-C functional species, respectively. After deactivation, new peaks at 284.1 and 288.2 eV appeared, corresponding to defective carbon and C=O (COOH, ketone) species, respectively^{39–41}. Moreover, the contents of C-OH and C-O-C markedly increased, as did the overall increase in oxygen content (Supplementary Fig. 11). These findings suggested a highly oxidized state of the graphite surface after deactivation, which was further substantiated by Fourier transform infrared (FTIR) spectroscopy analysis

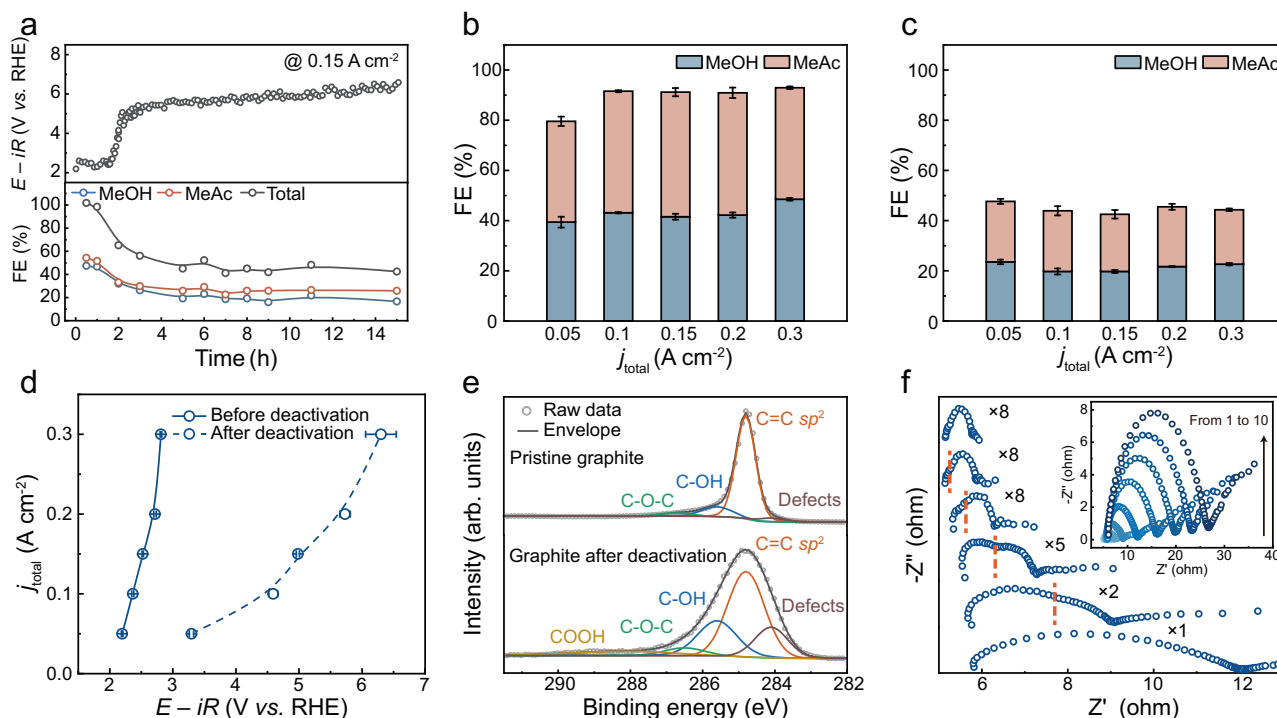


Fig. 1 | Investigation of the deactivation process involving a graphite electrode over an electrochemical decarboxylation reaction. **a** Potential and catalytic performance *versus* time profile for graphite at 0.15 A cm⁻² in an electrolyte containing 2 M NaAc and 2 M HAc (pH=4.75 ± 0.15). Catalytic performance of graphite at different current densities **(b)** pre-deactivation **(c)** post-deactivation. **d** The corresponding *j*-*V* curves of graphite before and after deactivation. **e** C 1s XPS spectra of pristine graphite and post-deactivated graphite. **f** Nyquist plots for the graphite reaction in 2 M NaAc and 2 M HAc at 2.47 V *vs.* RHE. The curves were

ascribed to cycles 1 to 6 from top to bottom, respectively, and each cycle was scanned in the range from 1 MHz to 0.1 Hz. The inset shows the curves of the scanning cycles from 1 to 10. The solution resistance (*R*) for **(a)** is around 20.1 Ω. The solution resistance (*R*) and the corresponding potential without *iR* correction for **(d)** can be found in the figure caption of Supplementary Fig. 17. The error bars correspond to the standard deviation of three independent measurements. Source data for this figure are provided in the Source Data file.

(Supplementary Fig. 12). Compared with the pristine material, the deactivated graphite exhibited a plethora of new peaks attributable to various functional groups, such as ethers ($\nu_{\text{C-O}}$ at 1033 cm⁻¹), carboxylic acid ($\nu_{\text{C-OH}}$ at 1219 cm⁻¹, δ_{OH} at 1443 cm⁻¹, $\nu_{\text{C=O}}$ at 1717 cm⁻¹), ketones ($\nu_{\text{C=O}}$ at 1630 cm⁻¹) and organic carbonate ($\nu_{\text{C=O}}$ at 1715 cm⁻¹, δ_{OH} at 1384 cm⁻¹)^{42,43}. These spectral features are indicative of the extensive oxidative modifications experienced by the graphite surface upon deactivation.

To verify the hypothesis that the oxidized graphite surface was the primary factor for the decrease in catalytic activity, we measured the deactivation behavior of graphite at various current densities. The correlation between graphite deactivation and the applied Coulomb charge was confirmed, as shown in Supplementary Fig. 13. The deactivated graphite was subsequently annealed at 900 °C in an Ar atmosphere to eliminate surface oxygen species⁴⁴ (Supplementary Fig. 14). The annealed graphite regained a low onset potential (below 3 V *vs.* RHE) for galvanostatic electrolysis at 0.3 A cm⁻², supporting the notion that deactivation was predominantly due to oxidation (Supplementary Fig. 15). Additionally, in-situ electrochemical impedance spectroscopy (EIS) measurements were conducted at 2.47 V *vs.* RHE, revealing the emergence and subsequent growth of a new inductive loop in the high-frequency domain (Fig. 1f). This new inductive loop was attributed to the dielectric oxidative graphite layer, which showed a similar trend for the formation of a solid-electrolyte interphase (SEI) in batteries, resulting in the inhibition of electron transfer. Taken together, we conclude that the deactivation of the graphite catalyst is ascribed to the formation of a fully oxidized surface layer, which obstructs the active sites with oxidized functional groups and hinders electron transfer, resulting in elevated reaction potentials and diminished catalytic performance.

Anion intercalation strategy for stable aqueous non-Kolbe electrolysis

Given the layered structure of graphite, it is widely adopted to enhance charge transfer through ion intercalation in the battery industry⁴⁵. We then sought to extend this strategy in-situ to address the passivation issue here for anodic catalysis (Fig. 2a). As expected, with the addition of 0.1 M NaClO₄, we observed rapid recovery of the anode potential from -6.5 to -2.9 V for the deactivated graphite in an electrolyte containing 2 M NaAc and 2 M HAc at a constant current density of 0.3 A cm⁻² (Fig. 2b). Subsequent evaluations of the catalytic performance for acetate decarboxylation, with the addition of 0.1 M NaClO₄ at various current densities, revealed that the total FE for non-Kolbe products (methanol and methyl acetate) exhibited trends comparable to those observed prior to passivation without the addition of anions. The liquid products presented a total FE of over 95% from 0.05 to 1 A cm⁻² (Fig. 2c). Gas products were quantified using GC and in-situ DEMS (Supplementary Fig. 16), which indicated a marked reduction in the production of CO, C₂H₆, and CO₂ when NaClO₄ was incorporated. The overlap of the *j*-*V* curves confirmed that the addition of NaClO₄ effectively maintained the superior performance of the graphite anode (Fig. 2d and Supplementary Fig. 17). The influence of NaClO₄ concentration on catalytic activity was found to be negligible, except when excessive perchlorate (>0.3 M) was added, which slightly impacted the catalytic activity, potentially due to excessive surface coverage (Supplementary Fig. 18). A stability test conducted at a constant current density of 0.15 A cm⁻² with the addition of 0.1 M NaClO₄ maintained the total FE for non-Kolbe products at ~95% over 130 h (Fig. 2e). Furthermore, the stability of the NaClO₄ system at a higher current density of 0.6 A cm⁻² showed no significant degradation over a period of 35 h (Supplementary Fig. 19).

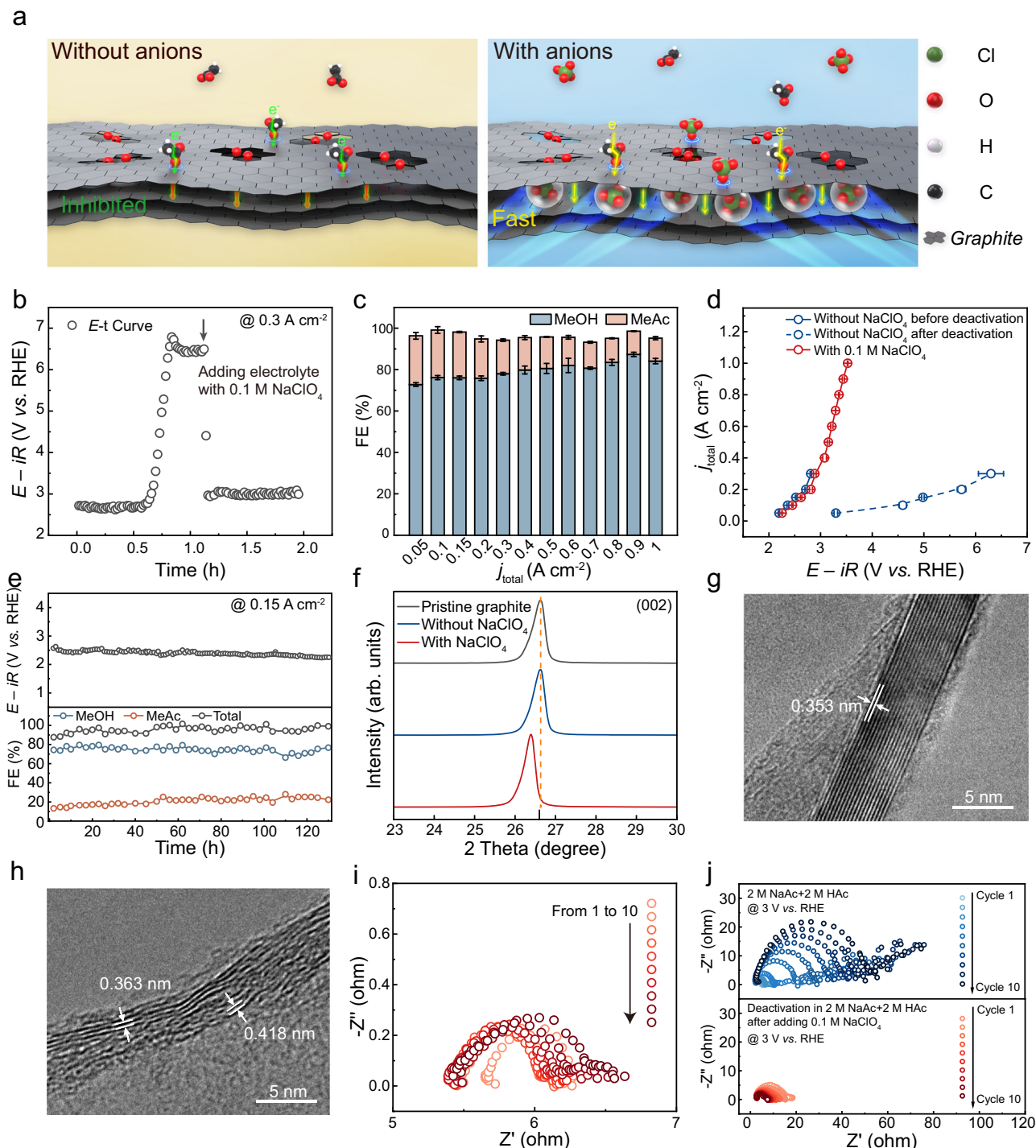


Fig. 2 | Strategy for reactivating a graphite electrode. **a** Schematic illustration of the reactivation strategy through the introduction of NaClO₄ into the electrolyte. **b** Potential vs. time curve at 0.3 A cm⁻² for deactivated graphite reacting in the electrolyte before and after the addition of 0.1 M NaClO₄. **c** FEs for non-Kolbe products at different current densities for graphite reacting in the electrolyte with 0.1 M NaClO₄. **d** The corresponding j -V curve of graphite reacting in the electrolyte with or without the addition of NaClO₄. **e** Stability test at 0.15 A cm⁻² in a flow cell system over 130 h. **f** XRD patterns of the graphite before and after reaction in the electrolyte with or without perchlorate. **g** HR-TEM images of graphite after reaction (g) without or (h) with NaClO₄. **i** Nyquist plots for the graphite reaction in 2 M NaAc

+ 2 M HAc with 0.1 M NaClO₄ at 2.47 V vs. RHE. The curves were ascribed to scanning cycles 1 to 10, and each cycle was scanned in the range from 1 MHz to 0.1 Hz. **j** Nyquist plots for the graphite reaction in 2 M NaAc + 2 M HAc and the subsequent addition of 0.1 M NaClO₄ at 3 V vs. RHE. The curves were ascribed to scanning cycles 1 to 10, and each cycle was scanned in the range from 1 MHz to 0.1 Hz. The solution resistance (R) for (b) is around 15.3 Ω . The solution resistance (R) and the corresponding potential without iR correction for (d) can be found in the figure caption of Supplementary Fig. 17. The solution resistance (R) for (e) is around 17.0 Ω . The error bars correspond to the standard deviation of three independent measurements. Source data for this figure are provided in the Source Data file.

The intercalation of perchlorate ions within the graphite layers was definitively demonstrated. The XRD patterns revealed a shift in the peak at 26.4° , corresponding to the (002) plane of graphitic carbon, to a lower degree, suggesting an expansion in the lattice structure⁴⁶ (Fig. 2f and Supplementary Fig. 20). SEM images confirmed that the layered structure of the graphite was well-maintained post-intercalation (Supplementary Figs. 21a, b). High-resolution transmission electron microscopy (HR-TEM) analysis revealed that the interlayer distance of the pristine graphite was around 0.342 nm (Supplementary Fig. 22). This distance increased to 0.353 nm following deactivation due to oxidation at elevated potentials, as shown in Fig. 2g. The intercalation of ClO_4^- induced a more pronounced increase to 0.418 nm (Fig. 2h). Further in-situ EIS measurements indicated that the shape of the Nyquist curves remained unchanged with increasing number of scan cycles, demonstrating the preservation of the electron transfer capabilities (Fig. 2i). We also measured the EIS spectra of the performance recovery of the deactivated graphite electrode with the addition of perchlorate, as shown in Fig. 2j. During electrocatalytic decarboxylation, charge transfer was hindered with increasing number of scan cycles, leading to an increase in the reaction overpotential. In stark contrast, the addition of NaClO_4 induced a rapid decrease in the charge transfer resistance. The charge transfer was further improved with increasing number of scan cycles. This result explained the instantaneous decrease in potential upon the addition of perchlorate shown in Fig. 2b and highlighted the effect of perchlorate on the increase in charge transfer.

We investigated the influence of NaClO_4 concentration and identified 0.02 M as the lowest perchlorate concentration for moderate recovery, despite a slight decrease in performance (Supplementary Fig. 23, detailed in Supplementary Note 2). Since non-Kolbe products (mainly olefins, alcohols, and esters) can be separated via distillation and solvent extraction, the remaining perchlorate is reusable (Supplementary Fig. 24 and Supplementary Note 3).

An anti-passivation effect was also observed for various anions, including nitrate (NaNO_3), sulfate (Na_2SO_4), and phosphate (Na_2HPO_4) (Supplementary Fig. 25a). XRD analysis revealed that the intensity of the (002) peak for all the anion-treated graphite samples decreased, indicating successful intercalation (Supplementary Fig. 26). However, the use of NaNO_3 , Na_2SO_4 , and Na_2HPO_4 resulted in a rapid decline in the FE for the total liquid products (Supplementary Figs. 25b–d). This decrease in performance is attributed to the instability of nitrate, sulfate, and phosphate ions under high anode potentials, which was further substantiated by iodometry experiments⁴⁷ (Supplementary Fig. 27). These findings suggest that while intercalation can mitigate passivation, the choice of anion is critical to maintaining the catalytic activity of graphite electrodes.

Insights for anion-induced selectivity improvement

Notably, the addition of NaClO_4 to the electrolyte enhanced methanol production, achieving a FE of approximately 80% (Fig. 2c) compared with the FE of 45% (Fig. 1b) observed with pristine graphite. This significant increase prompted a thorough investigation into the mechanisms underlying this selectivity enhancement. As shown in Fig. 3a, the molar ratios of methanol to methyl acetate exhibited a clear potential dependence in the presence of NaClO_4 . Specifically, at potentials below 2.8 V *vs.* RHE, the production of methanol is preferentially favored at higher NaClO_4 concentrations. Conversely, at potentials above 2.8 V *vs.* RHE, the NaClO_4 concentration appeared to have a less pronounced effect. Further analysis of different anions revealed that they also contributed to selectivity enhancement, but the impact was comparatively limited (Fig. 3b).

To study the evolution of surface species during electrolysis, in-situ attenuated total reflection surface-enhanced IR absorption spectroscopy (ATR-SEIRAS) was conducted (Fig. 3c, d). The vibrational peaks at 1237, 1367, 1438, and 1714 cm^{-1} were associated with acetic

acid, corresponding to $\nu_{\text{C=O}}$, $\delta_{\text{C-H}}$, $\delta_{\text{asC-H}}$, and $\nu_{\text{C=O}}$, respectively⁴⁸. In addition, the peaks at 1475 and 1556 cm^{-1} were assigned to the vibration of acetate. With increasing potential, there was a notable increase in the intensity of the acetic acid peaks and a decrease in the intensity of the acetate peaks, suggesting the consumption of carboxylate groups and the release of protons during the non-Kolbe reaction. The peak at 1400 cm^{-1} was ascribed to the O–C–O symmetric stretching (ν_{SOCO}) vibration of adsorbed acetate^{49,50}. Driven by the electric field, competitive adsorption occurred between the acetates and perchlorate anions on the graphite surface. Thus, the concentration of surface acetate in the NaClO_4 system appears to be significantly lower than that in the NaClO_4 -free system, as revealed by the faster decrease in the ν_{SOCO} peak when the potential increased, as shown in the inset of Fig. 3c, d. The adsorption of perchlorate anions can also be evidenced by the peak at 1120 cm^{-1} attributed to the stretching vibration of Cl-O^{51} . The observed increase in the intensity of the $\nu_{\text{Cl-O}}$ peak at lower potentials and its subsequent stabilization at potentials exceeding 2.07 V *vs.* RHE suggested that perchlorate adsorption intensified as the potential rose within the low range and reached a saturation point at higher potentials. This behavior corresponded well with the mole ratio changes illustrated in Fig. 3a, emphasizing the critical role of the adsorbed perchlorate concentration in selectivity regulation. The time-dependent ATR-SEIRAS experiments further supported this, as they showed a decrease in the ν_{SOCO} peak intensities, indicating the suppression of acetate adsorption (Fig. 3e, f). Additionally, electron paramagnetic resonance (EPR) analysis revealed that CH_3^* was the active radical during the reaction²⁵, providing deeper insight into the reaction mechanism (Supplementary Fig. 28).

Based on the above findings, we concluded that the selective production of methanol was predominantly influenced by the low surface concentration of acetate and the high surface concentration of perchlorate anions. Generally, acetate first adsorbs on the surface of catalysts and then loses an electron to form the CH_3COO^* intermediate (Supplementary Fig. 29). This intermediate then underwent decarboxylation, yielding adsorbed methyl (CH_3^*) and carbon dioxide. These CH_3^* ions subsequently preferentially lose an electron to become carbonium ions, which are then readily combined with nucleophiles such as H_2O , resulting in methanol, or with acetate, forming methyl acetate⁵². Therefore, a lower concentration of acetate on the surface hindered the formation of methyl acetate, favouring the production of methanol.

Extension of the anion intercalation strategy to other carboxylates

The comprehensive evaluation of the decarboxylation performance of graphite across various pH values and carboxylate concentrations underscores the broad effectiveness of the anion intercalation strategy (Fig. 4a, b, Supplementary Figs. 30–34). With the addition of perchlorate anions, the total FE of the graphite catalyst was greater than 90% for non-Kolbe products. This high efficiency was maintained across a range of conditions, with only a minor reduction to 80% under highly alkaline environments. Furthermore, the catalytic performance was well preserved for a long period when perchlorate ions were present, in stark contrast to the significant performance degradation observed in the absence of perchlorate.

The extension of the substrate scope to include C_{2+} carboxylates such as propionate and butyrate has yielded promising results (Supplementary Figs. 35–41 and Table S1). As shown in Fig. 4c, d and Supplementary Fig. 39, the presence of NaClO_4 in the electrolyte significantly mitigated the deactivation of graphite, maintaining a stable and low potential during constant current density electrolysis. For propionate decarboxylation, ethylene, generated by the elimination of hydrogen from carbonium ions, was identified as the main product, with an FE of over 40%²⁶. In the case of butyrate decarboxylation, the propyl carbonium ions undergo rearrangement, leading to

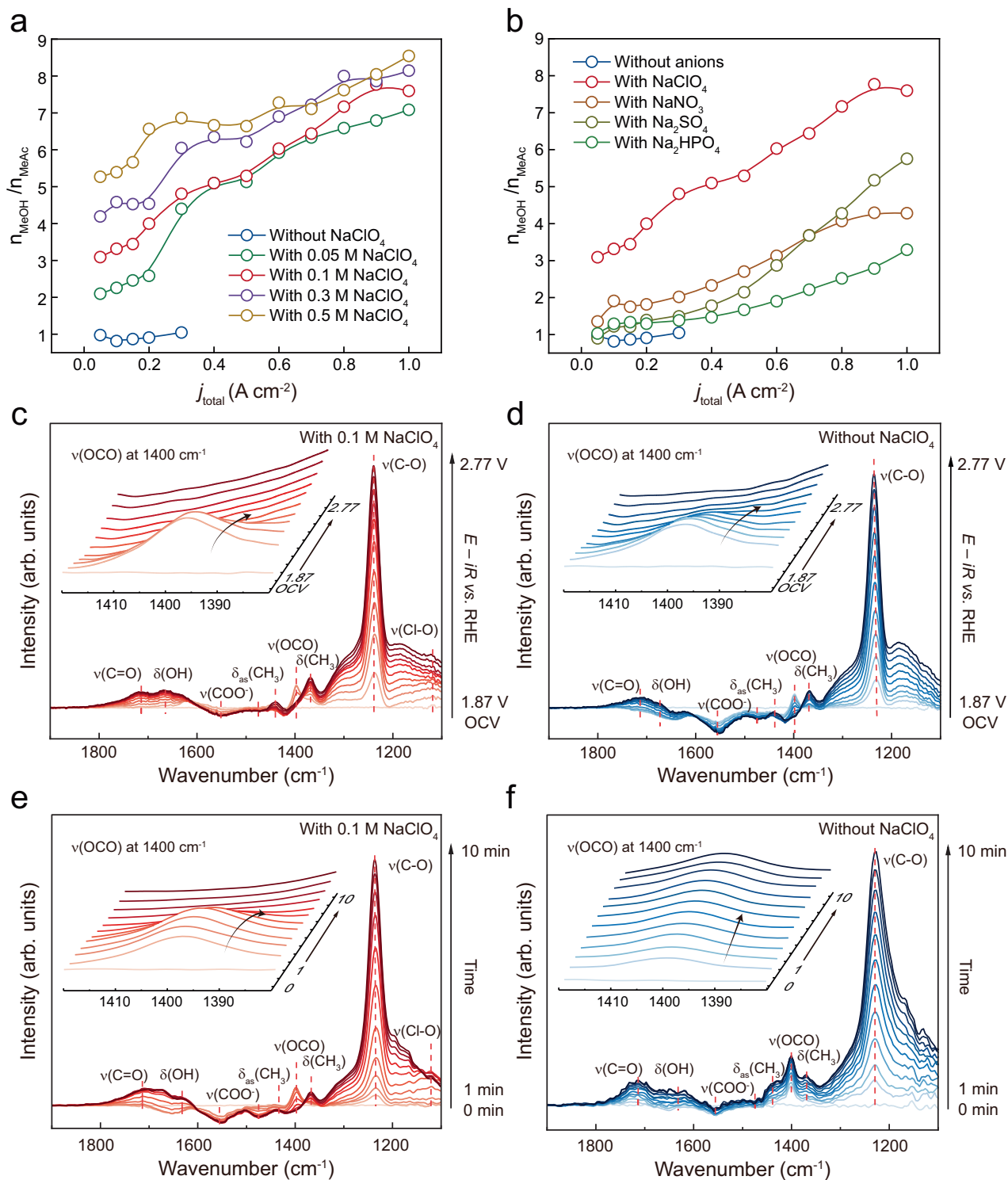
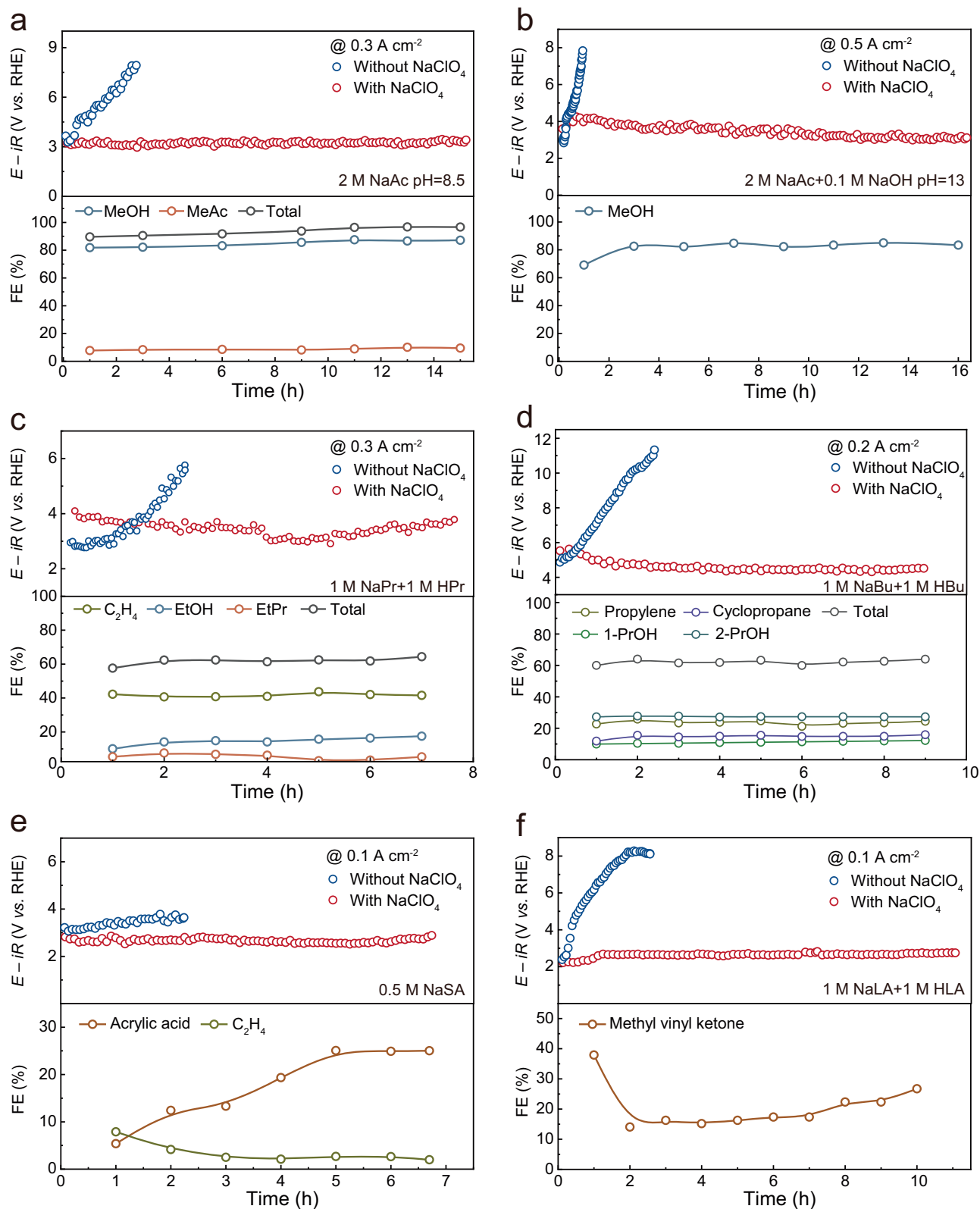


Fig. 3 | Influence of the addition of perchlorate on the distribution of non-Kolbe products. **a** The ratio of the non-Kolbe products with the addition of different concentrations of perchlorate. **b** The ratio of the non-Kolbe products with the addition of different anions. In-situ ATR-SEIRAS spectra of graphite reacting in the electrolyte **(c)** with or **(d)** without perchlorate with a change in potential. In-situ ATR-

SEIRAS spectra of graphite reacting in the electrolyte **(e)** with or **(f)** without perchlorate over time at 2.77 V vs. RHE. Changes in the intensity of the ν_{OCO} species are shown in the inset, which represents the adsorbed acetate. The solution resistance (R) for panels **(c)** and **(e)** is around 32.8Ω . The solution resistance (R) for **(d)** and **(f)** is around 34.3Ω . Source data for this figure are provided in the Source Data file.

the formation of 1- and 2-propanol⁵³. The corresponding j -V curves and FEs of the products of propionate and butyrate decarboxylation at different current densities were measured and are shown in Supplementary Fig. 40. In addition, the performance of octanoate (long-chain fatty carboxylate, carbon chain number ≥ 8) electrolysis with and without the addition of perchlorate was also evaluated

(Supplementary Fig. 41). These results suggest that the oxidation of the graphite electrode in the aqueous phase was inevitable. Like acetate electrolysis, perchlorate intercalation into graphite layers enhances charge transfer, lowering the reaction potential. The slight changes in product distribution were deduced to be due to the protective effect of the adsorbed long-chain carboxylate, as indicated by previous



studies³². Furthermore, widely used biomass carboxylates, such as succinate and levulinate, were also investigated, as shown in Fig. 4e, f and Supplementary Figs. 42–44. Olefins were identified as the main products. For succinate and levulinate decarboxylation, a stable and low potential was shown with the addition of NaClO₄, and the total FE of olefins (acrylic acid and ethylene for succinate and methyl vinyl ketone for levulinate) was maintained at ~20%. In contrast, in the

absence of NaClO₄, the potential apparently increased, and the catalytic performance decreased to below 10%. These findings suggest that with further refinement of strategies, such as precise control of the surface solvation environment, it may be possible to achieve even higher selectivity in these reactions.

In summary, we developed an anion intercalation strategy to realize the long-term stability of aqueous non-Kolbe electrolysis

Fig. 4 | Feasibility of the reactivating strategy under different conditions.

a Stability test of graphite reacting in an electrolyte containing 2 M NaAc (pH= 8.50 ± 0.25) with or without the addition of NaClO₄ at 0.3 A cm⁻². The solution resistance (R) is around 15.6 Ω and 16.7 Ω for the measurement with and without NaClO₄, respectively. **b** Stability test of graphite reacting in an electrolyte containing 2 M NaAc and 0.1 M NaOH (pH= 12.9 ± 0.20) with or without the addition of NaClO₄ at 0.5 A cm⁻². The solution resistance (R) is around 9.71 Ω and 9.5 Ω for the measurement with and without NaClO₄, respectively. **c** Stability test of graphite in an electrolyte containing 1 M propionic acid (HPr) and 1 M sodium propionate (NaPr) (pH= 4.88 ± 0.10) with or without the addition of NaClO₄ at 0.3 A cm⁻². The solution resistance (R) is around 24.9 Ω and 31.0 Ω for the measurement with and without NaClO₄, respectively. **d** Stability test of graphite in electrolyte containing

1 M butyric acid (HBu) and 1 M sodium butyrate (NaBu) (pH= 4.82 ± 0.25) with or without the addition of NaClO₄ at 0.2 A cm⁻². The solution resistance (R) is around 30.9 Ω and 38.5 Ω for the measurement with and without NaClO₄, respectively. **e** Stability test of graphite in an electrolyte containing 0.5 M monosodium succinate (NaSA) (pH= 6.50 ± 0.33) with or without the addition of NaClO₄ at 0.1 A cm⁻². The solution resistance (R) is around 36 Ω and 40.4 Ω for the measurement with and without NaClO₄, respectively. **f** Stability test of graphite in an electrolyte containing 1 M levulinic acid (HLA) and 1 M sodium levulinate (NaLA) (pH= 4.65 ± 0.13) with or without the addition of NaClO₄ at 0.1 A cm⁻². The solution resistance (R) is around 25.9 Ω and 28.1 Ω for the measurement with and without NaClO₄, respectively. The concentration ratio of carboxylate to NaClO₄ was maintained at 20:1 for all the tests.

using graphite as an anode catalyst. The introduced perchlorate ions sufficiently eliminated the inhibition of charge transfer resulting from the oxidation of the surface during electrolysis. Consequently, graphite exhibited an intrinsically high FE of ~95% for non-Kolbe products (methanol and methyl acetate) at wide current densities ranging from 0.05 to 1 A cm⁻². Furthermore, the intercalated graphite exhibited a preminent stability at 0.15 and 0.6 A cm⁻² over 130 and 35 h, respectively. In-situ spectroscopic analyses have shed light on the role of perchlorate in modulating the surface concentration of acetate, thereby enhancing the production of methanol. The applicability of this intercalation strategy was also successfully validated for the decarboxylation of propionate, butyrate, succinate, and levulinate. This study offers an efficient approach to address the longstanding challenge of catalyst passivation and provides a foundational framework for the development of catalysts with inherent high activity.

Methods

Chemicals

The graphite flake was purchased from Beijing Jingling Special Carbon Technology. Sodium acetate trihydrate, acetic acid, sodium hydroxide, sodium perchlorate monohydrate, sodium nitrate, sodium sulfate, sodium phosphate dibasic dihydrate, sulfuric acid, and 5,5-Dimethyl-1-pyrroline N-oxide (DMPO, 97%) were purchased from Aladdin. Graphite powder (D₅₀ < 400 nm, 99.95%), ethanol, propionic acid, and butyric acid were purchased from Macklin. Sodium propionate, sodium butyrate, succinic acid, levulinic acid, and Nafion (5 wt%) were purchased from Sigma-Aldrich. All the chemicals were used without further purification. Deionized (DI) water was used throughout the experiments. All the electrolyte solution was prepared by analytical balance and volumetric bottle before testing. All the solution was restored at room temperature.

Pretreatment of the graphite flake

The purchased graphite flake with a size of 0.5 mm × 10 cm × 10 cm was first cut into 1 cm × 2 cm pieces with blades. These pieces were subsequently ultrasonicated in 1 M diluted hydrochloric acid for 15 min, ethanol for 15 min, and water for 30 min in sequence to remove surface impurities. The washed pieces were dried in a vacuum oven at 60 °C for 12 h for further use.

Electrochemical measurements

All the electrochemical measurements and data collection were conducted by CHI (1140C) and Bio-Logic (VSP-3e) electrochemical workstations at room temperature. A customized reactor was used (Supplementary Fig. 2). The electrode area is 0.75 cm². Ag/AgCl (saturated KCl) was adopted as the reference electrode, and the counter electrode was a Pt-coated Ti mesh for the hydrogen evolution reaction. A carboxylate solution of 2 mL min⁻¹ was pumped into the anode side, and a 1 M H₂SO₄ solution of 2 mL min⁻¹ was pumped into the cathode side. The volume of the anodic and cathodic chambers is 5 mL. A Nafion 115 membrane (Fuel Cell Store) for cation

exchange was used. The membrane size was 1 cm × 2 cm with a thickness of 127 μm. Before testing, the Nafion membrane was treated by 5 wt.% H₂O₂ solution for 1 h at 80 °C. The treated membrane was subsequently treated by DI water, 1 M H₂SO₄ solution, and DI water for 1 h at 80 °C, respectively. Finally, the membrane was restored in DI water at room temperature for further use. A Nafion 115 membrane (Fuel Cell Store) was sandwiched by two gaskets between the anolyte and electrolyte to separate the chambers. All potentials were converted to the RHE reference scale using the following Eq. (1):

$$E_{\text{RHE}} = E_{\text{Ag/AgCl}} + 0.197 \text{ V} + 0.0591 \times \text{pH} \quad (1)$$

For reference electrode calibration, a Pt foil electrode covered with Pt black powder was adopted as a working electrode, the determined reference electrode, and a Pt wire as a counter electrode. 0.5 M H₂SO₄ was selected as the electrolyte for calibration. The pure hydrogen flow rate was maintained at 50 sccm for saturation to achieve 1 atm H₂ partial pressure. The CV data at a scan rate of 1 mV s⁻¹ indicate that the calibrated Ag/AgCl potential is 0.197 V *vs.* RHE.

The pH values of the electrolyte solution were measured by a high-accuracy pH benchtop meter (Mettler Toledo FiveEasy Plus FP20). The pH meter was calibrated by a three-point calibration method. The standard solutions with pH values of 4.00, 6.86, and 9.18 were used. Each value was measured three times.

The solution resistance (R) was determined by (PEIS) potentiostatic electrochemical impedance spectroscopy at frequencies ranging from 0.1 Hz to 200 kHz. All measured potentials were compensated by resistance with an 85% compensation coefficient unless otherwise mentioned.

Products analysis

The gas products were separated by a gas-liquid separator, and Ar was used as the carrier at a flow rate of 20 mL min⁻¹. Gas chromatography (GC, Agilent 8990) was used for the quantification of gas products. The FE of the gas products was calculated by the concentration detected by GC according to the following Eq. (2):

$$\text{FE}(\%) = \frac{nFxv_g}{V_m I} \times \frac{1}{60} \times 100\% \quad (2)$$

where *n* is the electron transfer number, *F* is the Faraday constant (96485 C mol⁻¹), *x* is the mole fraction of the gas products, *v_g* is the flow rate of gas (mL min⁻¹), *V_m* is the molar volume (24.5 L mol⁻¹ at 25 °C), and *I* is the applied current (A).

The liquid products were quantified by a 400 MHz NMR spectrometer (BRUKER). Then, 100 μL of D₂O (Sigma Aldrich, 99.9 at.%) and 0.05 μL of dimethyl sulfoxide (Sigma Aldrich, 99.9%) as an internal standard were added to 600 μL of the electrolyte after electrolysis. The FE of the liquid products was calculated by the concentration detected

by NMR according to the following Eq. (3):

$$\text{FE}(\%) = \frac{nFcv_l}{I} \times \frac{1}{60} \times 100\% \quad (3)$$

where n is the electron transfer number, F is the Faraday constant (96485 C mol^{-1}), c is the mole fraction of the liquid products, v_l is the flow rate of the liquid (ml min^{-1}), and I is the applied current (A).

The liquid products generated from the electrochemical decarboxylation of succinate were quantified by high-performance liquid chromatography (HPLC, PerkinElmer LC-300 system, America) equipped with a ROA-Organic Acid H^+ (8%) LC column. The measurements employed $5 \text{ mM H}_2\text{SO}_4$ as the mobile phase and were conducted at 60°C with a flow rate of 0.5 mL min^{-1} .

Characterization

X-ray diffraction (XRD) patterns were measured by a Philips X'Pert Pro Super diffractometer, and the standard λ value was 1.54178 \AA for Cu-K α radiation. The morphology of the samples was observed by scanning electron microscopy (SEM Gemini SEM 300) at an accelerating voltage of 5 kV . Raman spectra were obtained using a Renishaw inVia Raman analyser equipped with a 532 nm laser. X-ray photoelectron spectroscopy (XPS) measurements were conducted on a Kratos-Axis Supra XPS spectrometer, and the binding energies were corrected by referencing C $1s$ to 284.8 eV . High-resolution transmission electron microscopy (HRTEM) was carried out on a Tecnai G2 F20 S-TWIN using Mo-based TEM grids.

Ex-situ attenuated total reflection Fourier Transform Infrared Spectrometer absorption spectroscopy (ATR-FTIR)

Ex-situ ATR-FTIR data were collected with a Nicolet iS50 FT-IR spectrometer equipped with an iS50 built-in diamond ATR module. The graphite flakes were pressed tightly on a diamond prism. The wavenumber resolution was 4 cm^{-1} .

In-situ differential electrochemical mass spectrometry (DEMS) measurements

In-situ DEMS measurements were applied for the detection of the changes of gas products during the reaction, and the mass spectrometer was equipped with a capillary injection port. The gas was separated by a gas-liquid separator. The signals at mass-to-charge ratios of 27 and 44 were assigned to C_2H_6 and CO_2 , respectively.

In-situ electrochemical impedance spectroscopy (EIS) measurements

In-situ EIS measurements were conducted in a three-electrode system with a Bio-Logic (VSP-3e) electrochemical workstation. Pt wire was used as the counter electrode, and Ag/AgCl (saturated KCl) was used as the reference electrode. EIS measurements were acquired at an applied voltage of 2.47 V vs. RHE with an overlaid voltage of $\pm 20 \text{ mV}$. The frequency ranged from 1 MHz to 0.1 Hz .

In-situ attenuated total reflection surface-enhanced IR absorption spectroscopy (ATR-SEIRAS) measurements

In-situ ATR-SEIRAS spectra were collected with an FT-IR spectrometer (Thermo Scientific Nicolet iS50) equipped with an MCT-A detector. The Au-coated Si prism was prepared by evaporation. A 120 A current was used, and the Au film was deposited on the basal plane of a hemicylindrical Si prism with a thickness of 40 nm . The catalyst inks were prepared by mixing 5 mg of graphite powder ($<400 \text{ nm}$), 1 ml of ethanol, and $50 \mu\text{L}$ of ionomer. The Si prism was assembled in a spectroelectrochemical cell with Pt wire as the counter electrode and Ag/AgCl wire in a saturated KCl solution as the reference electrode. Electrolytes containing 2 M NaAc and 2 M HAc with or without the addition of 0.1 M NaClO_4 were used. All the spectra were collected at a resolution of

4 cm^{-1} , and each single-beam spectrum was an average of 200 scans. A Bio-Logic (VSP-3e) electrochemical workstation was used for potential control.

Electron paramagnetic resonance (EPR) measurements

The electrochemically generated methyl radical was performed in the electrolyte with 2 M acetate ($\text{pH} = 4.75$), and a three-electrode H-type cell was used. A graphite flake with dimensions of $1 \text{ cm} \times 1 \text{ cm}$ was used as the working electrode. A constant electrolysis current of 300 mA was adopted over 10 min due to the poor stability of DMPO under oxidative conditions. An in-situ trapping method was used as previously reported⁵⁴. Specifically, a pipette containing DMPO solution (200 mM , $400 \mu\text{L}$) was immersed in the electrode, and the tip was fully in contact with the surface of the graphite flake. The in-situ generated radicals were reacted with DMPO at the interface between the solution in the pipette and the surface. The final sample contained $400 \mu\text{L}$ of DMPO and $400 \mu\text{L}$ of electrolyte after the reaction and was named the DMPO + in-situ trapped solution. The sample, which was named the DMPO + before-electrolysis solution, contained $400 \mu\text{L}$ of DMPO and $400 \mu\text{L}$ of electrolyte before the reaction. All EPR measurements were taken at room temperature with an EPR spectrometer (JEOL JES-FA200).

Data availability

The authors declare that the data supporting the findings of this study are available within the paper and its Supplementary Information file. Source data are provided with this paper.

References

- Zheng, T. et al. Copper-catalysed exclusive CO_2 to pure formic acid conversion via single-atom alloying. *Nat. Nanotechnol.* **16**, 1386–1393 (2021).
- Overa, S. et al. Enhancing acetate selectivity by coupling anodic oxidation to carbon monoxide electroreduction. *Nat. Catal.* **5**, 738–745 (2022).
- Sullivan, K. P. et al. Mixed plastics waste valorization through tandem chemical oxidation and biological funneling. *Science* **378**, 207–211 (2022).
- Pichler, C. M., Bhattacharjee, S., Rahaman, M., Uekert, T. & Reisner, E. Conversion of polyethylene waste into gaseous hydrocarbons via integrated tandem chemical-photo/electrocatalytic processes. *ACS Catal.* **11**, 9159–9167 (2021).
- Zhou, H. et al. Selectively upgrading lignin derivatives to carboxylates through electrochemical oxidative C(OH)–C bond cleavage by a Mn-doped cobalt oxyhydroxide catalyst. *Angew. Chem. Int. Ed.* **60**, 8976 (2021).
- Nabil, S. K. et al. Acid-base chemistry and the economic implication of electrocatalytic carboxylate production in alkaline electrolytes. *Nat. Catal.* **7**, 330–337 (2024).
- Ullrich, J. & Breit, B. Selective hydrogenation of carboxylic acids to alcohols or alkanes employing a heterogeneous catalyst. *ACS Catal.* **8**, 785–789 (2018).
- Pritchard, J., Filonenko, G. A., Van Putten, R., Hensen, E. J. & Pidko, E. A. Heterogeneous and homogeneous catalysis for the hydrogenation of carboxylic acid derivatives: history, advances and future directions. *Chem. Soc. Rev.* **44**, 3808–3833 (2015).
- Xiang, J. et al. Hindered dialkyl ether synthesis with electro-generated carbocations. *Nature* **573**, 398–402 (2019).
- Zhang, B. et al. Ni-electrocatalytic Csp^3 – Csp^3 doubly decarboxylative coupling. *Nature* **606**, 313–318 (2022).
- Fawcett, A. et al. Photoinduced decarboxylative borylation of carboxylic acids. *Science* **357**, 283–286 (2017).
- Huang, Z. et al. Enhanced photocatalytic alkane production from fatty acid decarboxylation via inhibition of radical oligomerization. *Nat. Catal.* **3**, 170–178 (2020).

13. Akhade, S. et al. Electrocatalytic hydrogenation of biomass-derived organics: A review. *Chem. Rev.* **120**, 11370–11419 (2020).
14. Novaes, L. T. et al. Electrocatalysis as an enabling technology for organic synthesis. *Chem. Soc. Rev.* **50**, 7941–8002 (2021).
15. Faraday, M. Experimental researches in electricity. Seventh series. *Philos. Trans. R. Soc.* **124**, 77–122 (1833).
16. Kolbe, H. Untersuchungen über die Elektrolyse organischer Verbindungen. *Ann. Chem. Pharm.* **69**, 257–294 (1849).
17. Qiu, Y. et al. Electrocatalytic decarboxylation of carboxylic acids over RuO₂ and Pt nanoparticles. *Appl. Catal. B-Environ.* **305**, 121060 (2022).
18. Martínez, Á. M., Hayrapetyan, D., van Lingen, T., Dyga, M. & Gooßen, L. J. Taking electrodecarboxylative etherification beyond Hofer–Moest using a radical C–O coupling strategy. *Nat. Commun.* **11**, 4407 (2020).
19. Meyers, J. et al. Intramolecular biradical recombination of dicarboxylic acids to unsaturated compounds: a new approach to an old Kolbe reaction. *ChemElectroChem* **7**, 4873–4878 (2020).
20. Kingston, C. et al. A survival guide for the “electro-curious. *Accounts. Chem. Res.* **53**, 72–83 (2019).
21. dos Santos, T. R., Harnisch, F., Nilges, P. & Schroder, U. Electrochemistry for biofuel generation: transformation of fatty acids and triglycerides to diesel-like olefin/ ether mixtures and olefins. *ChemSusChem* **8**, 886–893 (2015).
22. Yu, J., Liu, T., Sun, W. & Zhang, Y. Electrochemical decarboxylative elimination of carboxylic acids to alkenes. *Org. Lett.* **25**, 7816–7821 (2023).
23. Kunugi, T. Electrolytic oxidation of salts of aliphatic acids by the Hofer–Moest Reaction. I. Formation of methanol from sodium acetate. *J. Am. Chem. Soc.* **75**, 1597–1599 (1953).
24. Kurig, N., Meyers, J., Holzhäuser, F. J., Palkovits, S. & Palkovits, R. (Non-) Kolbe chemistry going with the flow: the continuous electrolysis of biogenic acids. *ACS Sustain. Chem. Eng.* **9**, 1229–1234 (2020).
25. Pichler, C. M. et al. Bio-electrocatalytic conversion of food waste to ethylene via succinic acid as the central intermediate. *ACS Catal.* **12**, 13360–13371 (2022).
26. Garrido-Castro, A. F. et al. Scalable electrochemical decarboxylative olefination driven by alternating polarity. *Angew. Chem. Int. Ed.* **62**, e202309157 (2023).
27. Petrović, N. et al. Design of experiments-based optimization of an electrochemical decarboxylative alkylation using a spinning cylinder electrode reactor. *Org. Process Res. Dev.* **28**, 2928–2934 (2024).
28. Heard, D. M. & Lennox, A. J. (2020). Electrode materials in modern organic electrochemistry. *Angew. Chem. Int. Ed.* **59**, 18866–18884 (2020).
29. Stang, C. & Harnisch, F. The dilemma of supporting electrolytes for electroorganic synthesis: a case study on Kolbe electrolysis. *ChemSusChem* **9**, 50–60 (2015).
30. Liu, S., Govindarajan, N., Prats, H. & Chan, K. Understanding the reaction mechanism of Kolbe electrolysis on Pt anodes. *Chem Catal.* **2**, 1100–1113 (2022).
31. Ranninger, J., Nikolaienko, P., Mayrhofer, K. J. & Berkes, B. B. On-line electrode dissolution monitoring during organic electrosynthesis: direct evidence of electrode dissolution during Kolbe electrolysis. *ChemSusChem* **15**, e202102228 (2022).
32. Hintz, H. A. & Sevov, C. S. Catalyst-controlled functionalization of carboxylic acids by electrooxidation of self-assembled carboxyl monolayers. *Nat. Commun.* **13**, 1319 (2022).
33. Rueffer, M., Bejan, D. & Bunce, N. J. Graphite: an active or an inactive anode? *Electrochim. acta* **56**, 2246–2253 (2011).
34. Hioki, Y. et al. Overcoming the limitations of Kolbe coupling with waveform-controlled electrosynthesis. *Science* **380**, 81–87 (2023).
35. Ashraf, T., Rodriguez, A. P., Mei, B. T. & Mul, G. Electrochemical decarboxylation of acetic acid on boron-doped diamond and platinum-functionalised electrodes for pyrolysis-oil treatment. *Faraday Discuss* **247**, 252–267 (2023).
36. Timoshenko, J. et al. Steering the structure and selectivity of CO₂ electroreduction catalysts by potential pulses. *Nat. Catal.* **5**, 259–267 (2022).
37. Chen, W. et al. Pulse potential mediated selectivity for the electrocatalytic oxidation of glycerol to glyceric acid. *Nat. Commun.* **15**, 2420 (2024).
38. Lu, S. et al. Dissolution of the heteroatom dopants and formation of ortho-quinone moieties in the doped carbon materials during water electrooxidation. *J. Am. Chem. Soc.* **144**, 3250–3258 (2022).
39. Lu, S. et al. Phenanthrenequinone-like moiety functionalized carbon for electrocatalytic acidic oxygen evolution. *Chem* **8**, 1415–1426 (2022).
40. Lei, C. et al. High-performance metal-free nanosheets array electrocatalyst for oxygen evolution reaction in acid. *Adv. Funct. Mater.* **30**, 2003000 (2020).
41. Park, S. et al. Graphene oxide papers modified by divalent ions-enhancing mechanical properties via chemical cross-linking. *ACS Nano* **2**, 572–578 (2008).
42. Han, G. F. et al. Building and identifying highly active oxygenated groups in carbon materials for oxygen reduction to H₂O₂. *Nat. Commun.* **11**, 2209 (2020).
43. Wu, Q. et al. Unveiling the dynamic active site of defective carbon-based electrocatalysts for hydrogen peroxide production. *Nat. Commun.* **14**, 6275 (2023).
44. Figueiredo, J. L., Pereira, M. F. R., Freitas, M. M. A. & Orfao, J. J. M. Modification of the surface chemistry of activated carbons. *Carbon* **37**, 1379–1389 (1999).
45. Wang, G., Yu, M. & Feng, X. Carbon materials for ion-intercalation involved rechargeable battery technologies. *Chem. Soc. Rev.* **50**, 2388–2443 (2021).
46. Zhou, X. et al. Strategies towards low-cost dual-ion batteries with high performance. *Angew. Chem. Int. Ed.* **59**, 3802–3832 (2020).
47. Wang, J. & Wang, S. Reactive species in advanced oxidation processes: formation, identification and reaction mechanism. *Chem. Eng. J.* **401**, 126158 (2020).
48. Shao, M. H. & Adzic, R. R. Electrooxidation of ethanol on a Pt electrode in acid solutions: in situ ATR-SEIRAS study. *Electrochim. Acta* **50**, 2415–2422 (2005).
49. Ma, X. Y. et al. Revisiting the acetaldehyde oxidation reaction on a Pt electrode by high-sensitivity and wide-frequency infrared spectroscopy. *J. Phys. Chem. Lett.* **11**, 8727–8734 (2020).
50. Heinen, M., Jusys, Z. & Behm, R. J. Ethanol, acetaldehyde and acetic acid adsorption/electrooxidation on a Pt thin film electrode under continuous electrolyte flow: an in situ ATR-FTIRS flow cell study. *J. Phys. Chem. C* **114**, 9850–9864 (2010).
51. Yoon, I. H. et al. Perchlorate adsorption and desorption on activated carbon and anion exchange resin. *J. Hazard. Mater.* **164**, 87–94 (2009).
52. Holzhäuser, F. J., Mensah, J. B. & Palkovits, R. (Non-) Kolbe electrolysis in biomass valorization—a discussion of potential applications. *Green Chem.* **22**, 286–301 (2020).
53. Rangarajan, T. M., Velayutham, D. & Noel, M. Anodic oxidation of alkane carboxylates and perfluoroalkane carboxylates at platinum and graphite anodes: product selectivity and mechanistic aspects. *Ionics* **17**, 827–833 (2011).
54. Fan, L. et al. CO₂/carbonate-mediated electrochemical water oxidation to hydrogen peroxide. *Nat. Commun.* **13**, 2668 (2022).

Acknowledgements

J. Z. acknowledges the National Key Research and Development Program of China (2021YFA1500500), the CAS Project for Young Scientists

in Basic Research (YSBR-051), the NSFC (22221003, 22250007, 22361162655), the Science and Technology Development Fund (FDCT) of Macao S.A.R (0070/2023/AFJ), Fundamental Research Funds for the Central Universities, the Joint Fund of the Yulin University and the Dalian National Laboratory for Clean Energy (YLU-DNL Fund 2022012), the State Key Laboratory of Catalysis (2024SKL-A-01), and the International Partnership Program of Chinese Academy of Sciences (123GJHZ2022101GC). C. X. acknowledges the NSFC (52171201) and the Natural Science Foundation of Sichuan (2025NSFJQ0017). T. Z. acknowledges the NSFC (22322201, 22278067). X. L. acknowledges the Central Government Funds of Guiding Local Scientific and Technological Development for Sichuan Province (2024ZYD0152) and the Natural Science Foundation of Sichuan (2024NSFSC1107). L. L. acknowledges the NSFC (22309171). C. L. acknowledges the NSFC (22301031). Q. J. acknowledges the NSFC (22405035). J.Z. acknowledges support from the New Cornerstone Science Foundation through the XPLOER PRIZE. The authors appreciate the Analysis and Testing Center, University of Electronic Science and Technology of China, for their technical support. This work was partially carried out at the Instruments Center for Physical Science, University of Science and Technology of China.

Author contributions

The project was conceptualized and supervised by J.Z. and C.X.. X.Z. prepared the catalysts, performed the catalytic tests and in-situ electrochemical experiments with the help of C.L., W.X., D.Z., P.L., and X.F.. X.Z. and J.L. performed the catalyst characterizations. Y.J., T.Z., Q.J. and C.X. helped in the analysis of the data. X.Z., L.L., C.L., X.L., C.X., and J.Z. wrote the manuscript with input from all the authors. All the authors discussed the results and commented on the manuscript.

Competing interests

A China provisional patent application (202510190131.9) based on the technology described in this work was filed on Mar. 2025 by C.X., X.Z., X.L., X.F., Q.J., and T.Z. at the University of Electronic Science and Technology of China. The other authors declare no competing interests.

Additional information

Supplementary information The online version contains supplementary material available at <https://doi.org/10.1038/s41467-025-58924-x>.

Correspondence and requests for materials should be addressed to Chuan Xia or Jie Zeng.

Peer review information *Nature Communications* thanks Xitao Liu and the other, anonymous, reviewer(s) for their contribution to the peer review of this work. A peer review file is available.

Reprints and permissions information is available at <http://www.nature.com/reprints>

Publisher's note Springer Nature remains neutral with regard to jurisdictional claims in published maps and institutional affiliations.

Open Access This article is licensed under a Creative Commons Attribution-NonCommercial-NoDerivatives 4.0 International License, which permits any non-commercial use, sharing, distribution and reproduction in any medium or format, as long as you give appropriate credit to the original author(s) and the source, provide a link to the Creative Commons licence, and indicate if you modified the licensed material. You do not have permission under this licence to share adapted material derived from this article or parts of it. The images or other third party material in this article are included in the article's Creative Commons licence, unless indicated otherwise in a credit line to the material. If material is not included in the article's Creative Commons licence and your intended use is not permitted by statutory regulation or exceeds the permitted use, you will need to obtain permission directly from the copyright holder. To view a copy of this licence, visit <http://creativecommons.org/licenses/by-nc-nd/4.0/>.

© The Author(s) 2025